# Constraints on mineralization, fluid-rock interaction, and mass transfer during faulting at 2–3 km depth from the SAFOD drill hole

Anja M. Schleicher,[1,2] Sara N. Tourscher,[1] Ben A. van der Pluijm,[1] and Laurence N. Warr[3]

[1]   Mineralogical and geochemical changes in mudrock cuttings from two segments of the San Andreas Fault Observatory at Depth (SAFOD) drill hole (3066–3169 and 3292–3368 m measured depth) are analyzed in this study. Bulk rock samples and hand-picked fault-related grains characterized by polished surfaces and slickensides were investigated by X-ray diffraction, electron microscopy, and geochemical analysis. The elemental changes in fault-related grains along the sampled San Andreas Fault are attributed to dissolution of detrital grains (particularly feldspar and quartz) and local precipitation of illite-smectite and/or chlorite-smectite mixed layers in fractures and veins. Assuming $ZrO_2$ and $TiO_2$ to be immobile elements, systematic differences in element concentrations show that most of the elements are depleted in the fault-related grains compared to the wall rock lithology. Calculated mass loss between the bulk rock and picked fault rock ranges from 17 to 58% with a greater mass transport in the shallow trace of the sampled fault that marks the upper limit the fault core. The relatively large amount of element transport at temperatures of $\sim$110–114°C recorded throughout the core requires extensive fluid circulation during faulting. Whereas dissolution/precipitation may be partly induced by the disequilibrium between fluids and rocks during diagenetic processes, stress-induced dissolution at grain contacts is proposed as the main mechanism for extensive mineral transformation in the fault rocks and localization of neomineralization along grain interface slip surfaces.

**Citation:** Schleicher, A. M., S. N. Tourscher, B. A. van der Pluijm, and L. N. Warr (2009), Constraints on mineralization, fluid-rock interaction, and mass transfer during faulting at 2–3 km depth from the SAFOD drill hole, *J. Geophys. Res.*, *114*, B04202, doi:10.1029/2008JB006092.

## 1.  Introduction

[2]   Fluids associated with the formation of clay minerals are increasingly recognized as an important factor in shallow crustal faulting at depths of <10 km [*Wu et al.*, 1975; *Carter et al.*, 1990; *Sibson*, 1994; *Vrolijk and van der Pluijm*, 1999]. Their circulation along faults and shear zones can enhance mineral dissolution, element transport, mineral precipitation and rock deformation, depending on the temporal and spatial variations in temperature, pressure and element activities [*Beach*, 1976; *Hulsebosch and Frost*, 1989; *Manatschal et al.*, 2000; *Hayman*, 2006]. At low temperatures, such dynamic changes often lead to the crystallization of hydrous clay minerals in the faulted host rock, which influences permeability and fluid flow, and can transform the fault into a fluid barrier. Potential sources of fluids in shallow faults include meteoric, connate, basinal, metamorphic, and hydrothermal waters [*McCaig*, 1984, 1997; *Forster and Evans*, 1991; *Marquer and Burkhard*, 1992]. Whereas fluids in faults and fractures play a key role in the formation of clay minerals and vice versa [*Dewhurst et al.*, 1999; *Tobin et al.*, 2001; *Crawford et al.*, 2002; *Schleicher et al.*, 2006a], the precise role of fluid-rock interaction and associated clay formation in fault zones is not sufficiently understood [*Chester and Logan*, 1986; *Evans and Chester*, 1995].

[3]   This paper presents comprehensive geochemical data from hand-picked, fine-grained fault rock cuttings and equivalent mudrock lithologies of the wall rock, sampled at various depths from the SAFOD drill hole. Data collected in this study demonstrate the extent of mineralization and element transport, and describe the fluid-rock interactions in fault rocks and their host lithologies in the deep San Andreas Fault. Two areas of primary interest were targeted for this study (Figure 1c): a shallow fault trace (fault trace 1) between 3066 m and 3169 m measured depths (MD) and the main trace between 3292 m and 3368 m MD (fault trace 2). The $\sim$100 m wide shallow fault section is interpreted as a fault zone on the basis of rock deformation and alteration features [*Bradbury et al.*, 2007; *Solum et al.*, 2006]. This zone lays $\sim$25 m above a level of active casing deformation located at 3194 m [*Hickman et al.*, 2008]. The $\sim$75 m wide main fault trace includes the active fault recognized by

[1]Department of Geological Sciences, University of Michigan, Ann Arbor, Michigan, USA.
[2]Geozentrum Nordbayern, Friedrich Alexander Universität Erlangen-Nürnberg, Erlangen, Germany.
[3]Institut für Geographie und Geologie, Ernst Moritz Arndt Universität Greifswald, Greifswald, Germany.
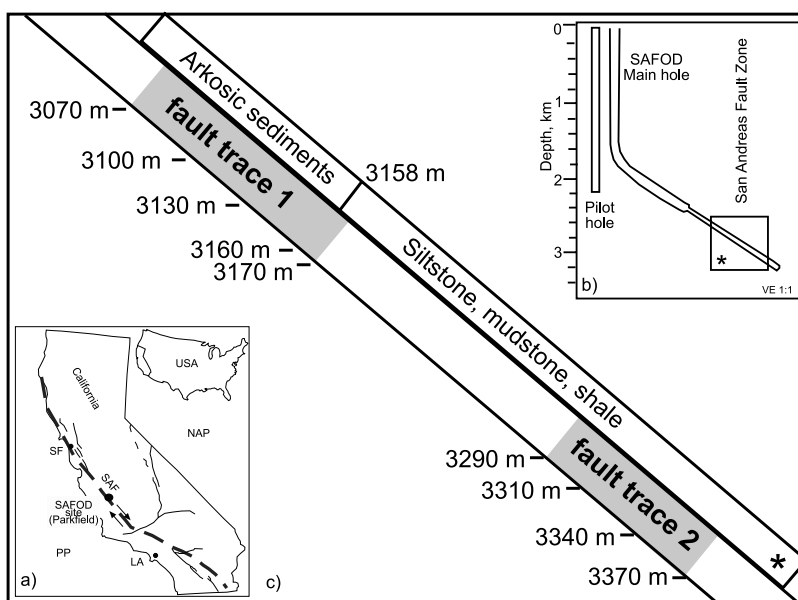
**Figure 1.** (a) Location map marking the San Andreas Fault and the San Andreas Fault Observatory at Depth (SAFOD) drill site in Parkfield. (b) Schematic image of the SAFOD drill holes (Pilot hole and Main hole) modified after *Zoback and Hickman* [2005]. (c) Details of the study area, showing the main lithologies and the sample location of the shallow fault trace 1 (3069 to 3170 m measured depth (MD)) and the deep main fault trace 2 (3292 to 3368 m MD), modified after *Draper et al.* [2005]. SF, San Francisco; LA, Los Angeles; PP, Pacific Plate; NAP, North American Plate; SAF, San Andreas Fault.

casing deformation at 3301 m MD [*Zoback et al.*, 2005]. The elemental geochemistry of 10 major and 3 minor elements for 36 fault rock samples, for 27 host rock samples and for 21 crushed bulk rock samples were analyzed. As prior observations showed that fault-related smectitic clay grows during slip as thin films on fracture surfaces and that matrix clay minerals of a burial diagenetic origin character-ize the host mudrocks [*Schleicher et al.*, 2006a, 2009], it was critical to select the small fragments of mineralized fault rock from the cuttings in order to examine the fault rock geochemistry.

[4] Both bulk mineral assemblages and elemental com-position of exhumed rocks of the San Andreas Fault have been previously reported [e.g., *Evans and Chester*, 1995; *Solum et al.*, 2006; *Schulz and Evans*, 2000]. However, this paper is the first to present SAFOD geochemical data from the fault rocks at depths, including the creeping part of the San Andreas Fault, as opposed to bulk rock analyses that mask fault-related processes. We present evidence that significant volumes of fluids have circulated through the fault zone over its history of development, despite the apparent lack of present-day evidence for fluid flow based on drilling mud-gas analyses [*Wiersberg and Erzinger*, 2007, 2008].

## 2. San Andreas Fault and the SAFOD Drill Hole

[5] The ~1300 km long San Andreas Fault is a right-lateral strike-slip fault in western California, marking the boundary between the Pacific Plate in the west and the North American Plate in the east (Figure 1a). In the area of Parkfield in central California, the fault transitions from creeping to seismic behavior, resulting in enhanced major

and minor earthquakes at different depths. For this reason, a hole has been drilled through the San Andreas Fault at this location (the San Andreas Fault Observatory at Depth (SAFOD)) as part of the Earthscope initiative (http://www.icdp-online.de/sites/sanandreas/index/). This hole, sit-uated ~1.8 km southwest of the surface trace of the fault, provides a natural laboratory to study the physical and chemical processes associated with active deformation, creep and earthquake generation [*Hickman et al.*, 2004]. In 2002, a vertical Pilot hole was drilled to 2.2 km depth into Salinian granite and granodiorite after passing through pebbly sandstone [*Hickman and Zoback*, 2004; *Solum and van der Pluijm*, 2004]. The main hole, drilled during 2004 and 2005 (phases 1 and 2), is vertical to a depth of approximately 1.7 km, where it begins an angled descent in order to intersect the trace of the San Andreas Fault at around 2.7 km true vertical depth (TVD; Figure 1b). Phase 1 was completed in 2004 and drilled through Quaternary and Tertiary sedimentary rocks, granite/granodiorite and into arkosic sedimentary rocks [*Draper et al.*, 2005; *Hickman et al.*, 2005]. Phase 2 activities occurred in summer 2005 and completed drilling to 3992 m measured depth (MD) along the drill hole. This drilling extended into interbedded mudstone, siltstone and shale lithologies at the bottom of the drill hole (Figure 1c) [*Draper et al.*, 2005; *Hickman et al.*, 2005]. *Bradbury et al.* [2007] investigated the bulk miner-alogy of the SAFOD drill cuttings, showing an arkosic rock sequence from 1920 to 2550 m, separated by a clay rich zone at 2530–2680 m and a fine-grained sequence at 2680–3150 m MD. A lithologic change occurs at ~3150 m MD, where arenites are replaced by fine-grained siltstone and shaly fragments. The section at 3150–3550 m MD is characterized by fine-grained quartz-feldspar-rich mudrocks

**Table 1.** Calculated Mass Change and Calculated Mass Transport in Sections A–D of Figure 6

| | 3069–3158 m (MD) | | 3161–3170 m (MD) | | 3292–3316 m (MD) | | 3319–3368 m (MD) | |
|---|---|---|---|---|---|---|---|---|
| | Oxide Calculated Mass Change (%) | Calculated Mass Transport (g/100 g) | Oxide Calculated Mass Change (%) | Calculated Mass Transport (g/100 g) | Oxide Calculated Mass Change (%) | Calculated Mass Transport (g/100 g) | Oxide Calculated Mass Change (%) | Calculated Mass Transport (g/100 g) |
| Al2O3 | −43.7 | −6.10 | −12.7 | −1.58 | −6.0 | −0.59 | 6.4 | 0.86 |
| BaO | −91.7 | −0.23 | −80.9 | −0.12 | −72.2 | −0.07 | −58.4 | −0.05 |
| CaO | −61.0 | −1.13 | −67.7 | −2.20 | −69.0 | −3.05 | −63.9 | −1.81 |
| Fe2O3 | −18.2 | −0.58 | −13.4 | −0.54 | −28.3 | −1.19 | 10.7 | 0.55 |
| K2O | −39.6 | −1.29 | −13.7 | −0.34 | −16.9 | −0.32 | −9.4 | −0.21 |
| MgO | 50.1 | 0.29 | 1.8 | 0.02 | −21.6 | −0.49 | 3.0 | 0.09 |
| MnO | 16.6 | 0.01 | −43.0 | −0.02 | −64.3 | −0.05 | −28.6 | −0.02 |
| Na2O | −70.5 | −2.17 | −41.0 | −0.61 | −41.4 | −0.61 | −13.9 | −0.25 |
| P2O5 | 170.8 | 0.03 | −3.3 | 0.00 | 19.8 | 0.05 | −10.1 | −0.02 |
| Rb2O | −16.6 | −0.01 | −22.2 | 0.00 | −8.3 | 0.00 | 8.3 | 0.00 |
| SiO2 | −64.4 | −47.22 | −31.3 | −23.20 | −41.4 | −31.18 | −22.6 | −16.00 |
| TiO2 | 26.3 | 0.09 | 3.6 | 0.02 | 11.7 | 0.04 | 19.6 | 0.09 |
| ZrO2 | −10.7 | 0.00 | −7.1 | 0.01 | −22.4 | 0.00 | −1.7 | 0.00 |
| Sum | | −58.34 | | −28.56 | | −37.46 | | −16.77 |

(siltstone and shales) with interbedded sandstones. The occurrence of localized alteration and cataclasite defines multiple deformation zones in the 3000–3400 m MD region. In summer 2007, Phase 3 was completed by drilling several multilateral core holes from the main hole within the active segment of the San Andreas Fault.

## 3. Methods

[6] Drill cuttings, a few mm in size, were selected in 3 m intervals for systematic analysis from the two sections of the San Andreas Fault drill hole; the shallower fault trace 1 (3066 m to 3169 m MD), and the deeper main fault trace 2 (3292 m to 3368 m MD). A magnet was used to separate steel shavings from each sample introduced during drilling. The remaining cuttings were examined under a binocular microscope with the purpose of identifying and picking fault-related grains. Hand-picked grains allow detailed characterization of the fault rock minerals and recognition of small-scale heterogeneities that are associated with faulting. The dark gray fault fragments are typical mudrocks (siltstones, mudstones, and clay stones), mainly less than 1 mm in size and identified by the presence of polished surfaces and thin film coatings with slickenside striations. For each sample, approximately 100–200 mg of material was hand-picked and rinsed for ~1 min in deionized water in an ultrasonic bath to remove any remaining drilling mud and steel shaving contamination.

[7] The mineral assemblages of the bulk mudrock and the picked fault-related grains were determined using a Scintag X-ray diffractometer with CuK$\alpha$ radiation and a step size of 0.02 °2$\theta$. The preparation of the rock samples followed the analytical methods described by *Moore and Reynolds* [1997]. Randomly oriented powder samples, as well as oriented samples (air-dried and ethylene glycolated) were prepared to identify the individual bulk and clay mineralogy. For scanning electron microscopy (SEM) analysis, polished thin sections from core material at 3066 m and 3436 m MD were coated with carbon and studied with a Hitachi S3200N SEM using backscatter imaging and semi-quantitative energy (X-ray) dispersive spectroscopy (EDS).

The mineral occurrence, composition and shape were characterized from 3 m above fault trace 1, and from approximately 68 m below fault trace 2. These representative mudrock samples were chosen because of their best proximity to the areas of interest.

[8] Elemental geochemistry including major rock forming elements and some minor elements (Rb, Ti, and Zr) of the bulk rock and the picked fault rock samples were analyzed using Inductively Coupled Plasma-Optical Emission Spectrometry (ICP-OES). The powdered rock samples (100 mg) were digested in 5% trace metal $HNO_3$ with 1 g of ultra pure fused anhydrous lithium metaborate and 100 mg of lithium bromide (a nonwetting agent was included to facilitate melting). A Mn solution was used to align the ICP-OES. The ICP-OES was calibrated using a blank and 6 dilutions (1/10, 1/50, 1/100, 1/500, 1/1000, and 1/5000) of SM-225102, a certified digest standard (High Purity Standards). Quality control samples, River sediment B, Trace Metal Drinking Water, and SM-90 were chosen as they include all of the elements analyzed. They were measured after every ten samples to check for instrument drift. USGS standards QLO-1, RGM-1, SCo-1, BHVO-1, and SDC-1 [*Abbey*, 1983; *Gladney and Roelandts*, 1988; *Govindaraju*, 1994; *Flanagan*, 1976] were also analyzed and used to routinely correct measurements.

[9] Modifying *Gresens'* [1967] and *Grant's* [1986, 2005] volume composition calculations, the following mass balance equations can be written for four sections of the fault (3069–3158 m, 3160–3170 m, 3292–3316 m, 3320–3368 m) on the basis of changes in element distribution. In order to determine the percent change of each oxide, the slope is used to predict where the plucked fault concentration of a given oxide should lie along the slope of immobile oxides and the differences between the actual and the predicted measurement established. The amount of element gain or loss is determined by multiplying the percent change and the bulk rock value (Table 1). For the purpose of this study, the ratio of the density of wall rock to fault rock is assumed to be 1, reflecting the observations that the rock types are similar. Using the percent change for each element

(Table 1), the amount of each element lost per 100 g of bulk rock is calculated below:

$$100 \text{ g bulk rock} - 47.22 \text{ g SiO}_2 - 6.10 \text{ g Al}_2\text{O}_3 - 2.17 \text{ g Na}_2\text{O}$$
$$- 1.29 \text{ g K}_2\text{O} - 1.13 \text{ g CaO} - 0.58 \text{ g Fe}_2\text{O}_3 - 0.23 \text{ g BaO}$$
$$- 0.01 \text{ g Rb}_2\text{O} = 41.27 \text{ g fault rock} + 0.29 \text{ g MgO}$$
$$+ 0.09 \text{ g TiO}_2 + 0.03 \text{ g P}_2\text{O}_5$$
$$+ 0.01 \text{ g MnO } (3066 - 3158 \text{ m MD})$$

$$100 \text{ g bulk rock} - 23.20 \text{ g SiO}_2 - 2.20 \text{ g CaO} - 1.58 \text{ g Al}_2\text{O}_3$$
$$- 0.61 \text{ g Na}_2\text{O} - 0.54 \text{ g Fe}_2\text{O}_3 - 0.34 \text{ g K}_2\text{O} - 0.12 \text{ g BaO}$$
$$- 0.02 \text{ g MnO} = 71.39 \text{ g fault rock} + 0.02 \text{ g TiO}_2$$
$$+ 0.02 \text{ g MgO } (3161 - 3169 \text{ m MD})$$

$$100 \text{ g bulk rock} - 31.18 \text{ g SiO}_2 - 3.05 \text{ g CaO} - 1.19 \text{ g Fe}_2\text{O}_3$$
$$- 0.59 \text{ g Al}_2\text{O}_3 - 0.61 \text{ g Na}_2\text{O} - 0.49 \text{ g MgO} - 0.32 \text{ g K}_2\text{O}$$
$$- 0.07 \text{ g BaO} - 0.5 \text{ g MnO} = 61.99 \text{ g fault rock} + 0.04 \text{ g TiO}_2$$
$$+ 0.05 \text{ P}_2\text{O}_5 (3292 - 3316 \text{ m MD})$$

$$100 \text{ g bulk rock} - 16.00 \text{ g SiO}_2 - 1.81 \text{ g CaO} - 0.25 \text{ g Na}_2\text{O}$$
$$- 0.21 \text{ g K}_2\text{O} - 0.05 \text{ g BaO} - 0.02 \text{ g MnO}, - 0.02 \text{ g P}_2\text{O}_5$$
$$= 81.6 \text{ g fault rock} + 0.86 \text{ g Al}_2\text{O}_3 + 0.55 \text{ g Fe}_2\text{O}_3 + 0.09 \text{ g MgO}$$
$$+ 0.09 \text{ g TiO}_2 (3219 - 3368 \text{ m MD})$$

## 4. Results

### 4.1. Mineralogy

#### 4.1.1. X-Ray Diffraction Analysis

[10] The X-ray diffraction (XRD) analyses of randomly oriented bulk rock samples show abundant quartz, feldspar (both plagioclase and K-feldspar) and clay minerals (illite and illite-smectite/I-S) as main components, along with minor amounts of calcite and laumontite in some samples [see also *Solum et al.*, 2006]. The appearance of chlorite and chlorite-smectite (C-S) minerals at ~3150 m MD reflects the lithologic change from finer grained arkosic sandstones to a fine-grained quartz-feldspar-rich siltstone that alternates with sandy and shaly sections [*Draper et al.*, 2005; *Bradbury et al.*, 2007]. The picked fault-related grain material comprises fine-grained mudrock lithologies containing abundant illite and I-S along with quartz and plagioclase components in the shallow fault trace. Occasional discrete smectite minerals with additional chlorite and/or C-S also occur in the deeper fault trace. Because the fault and matrix mineralization cannot be entirely separated, the basic fault rock mineralogy is not significantly different from the bulk wall rock assemblage, except of the higher abundance of smectite components in the I-S and C-S mix-layered minerals. Notable variations in the abundance of chlorite, illite, I-S and C-S from the picked fault rocks at different depths were observed on the basis of air-dried and glycolated XRD patterns of oriented samples.

[11] Three representative samples from the shallow fault trace 1 and the deeper fault trace 2 are shown in Figures 2a–2c. The low-angle diffraction pattern at 3075 m MD (Figure 2a) shows a broad peak in the air-dried sample with two distinct maxima, caused by the combined contribution of two >10 Å phases. The peak at ~10 Å represents a pure illite phase, whereas the peak at ~11 Å indicates the I-S phase. A shift to ca 12 Å after saturation with ethylene glycol reflects a small amount of interlayer smectite [*Moore and Reynolds*, 1997; *Schleicher et al.*, 2009]. The XRD patterns of the fault-related grains at 3170 m MD that reflects the deepest sample in the shallow area (Figure 2b), shows as well typical illite and I-S components in the form of a broad peak with two maxima. However, here the I-S peak occurs at 10.6 Å, reflecting fewer smectite interlayers. The glycolated mixed-layered reflection is likely obscured by the position of the chlorite peak at 14.5 Å.

[12] The fault rocks from fault trace 2 shows similar components of illite and I-S. However, on the basis of the peak shape and peak position, I-S with slightly higher amounts of smectite occurs in some of the samples, as seen, for example, at 3344 m MD (Figure 2c) with a broad I-S peak shifting to 12.6 Å after ethylene glycolation. The shift of the chlorite peak in the glycolated samples indicate a C-S phase that could be observed in most of the XRD patterns at these depths. Similar C-S mixed-layered phases were described from the exhumed Punchbowl fault and the SAFOD Pilot hole [*Solum et al.*, 2003; *Solum and van der Pluijm*, 2004].

#### 4.1.2. Scanning Electron Microscopy Analysis

[13] To image the minerals and microstructures of the investigated mudrocks and to obtain confirmation of the mineral assemblages determined by XRD, Figure 3 presents representative backscattered electron images from two rock core samples at 3066 m MD (~3 m above the shallow trace) and 3436 m MD (68 m below the main trace). Numerous reaction textures are observed with quartz, feldspar, chlorite, illite and associated mixed-layered clays along the investigated fault traces 1 and 2 (Figures 3a and 3b). K-feldspar and albite/anorthite detrital clasts are strongly dissolved, and associated pores and sutured grain boundaries are often filled with clay minerals that make up the fine-grained matrix of these fine-grained clastic lithologies. Pores formed within grains occur in both quartz and feldspar, whereby the strongly dissolved plagioclase (albite/anorthite mixtures) appears only as isolated remnants occurring within the clay dominated matrix. Relatively large (>2 $\mu$m) detrital grains of illite occur together with <2 $\mu$m authigenic I-S particles with characteristic irregular flaky shapes [*Schleicher et al.*, 2009]. Figure 3a shows albite/anorthite minerals from the shallower sample at 3066 m MD altered into I-S clay minerals. The EDS patterns of the alteration products show a relatively high amount of K and less Na and Ca, next to Mg and less Fe. Also, I-S precipitates in small pores are relatively K rich.

[14] The more fractured minerals in the deeper samples at 3436 m MD (Figure 3b) show even stronger alteration of detrital plagioclase, feldspar and quartz, with enhanced mineralization of mixed-layered I-S as well as C-S minerals with a range of different particle sizes and shapes. Irregular fractures and veins are mainly filled with calcite, but on the
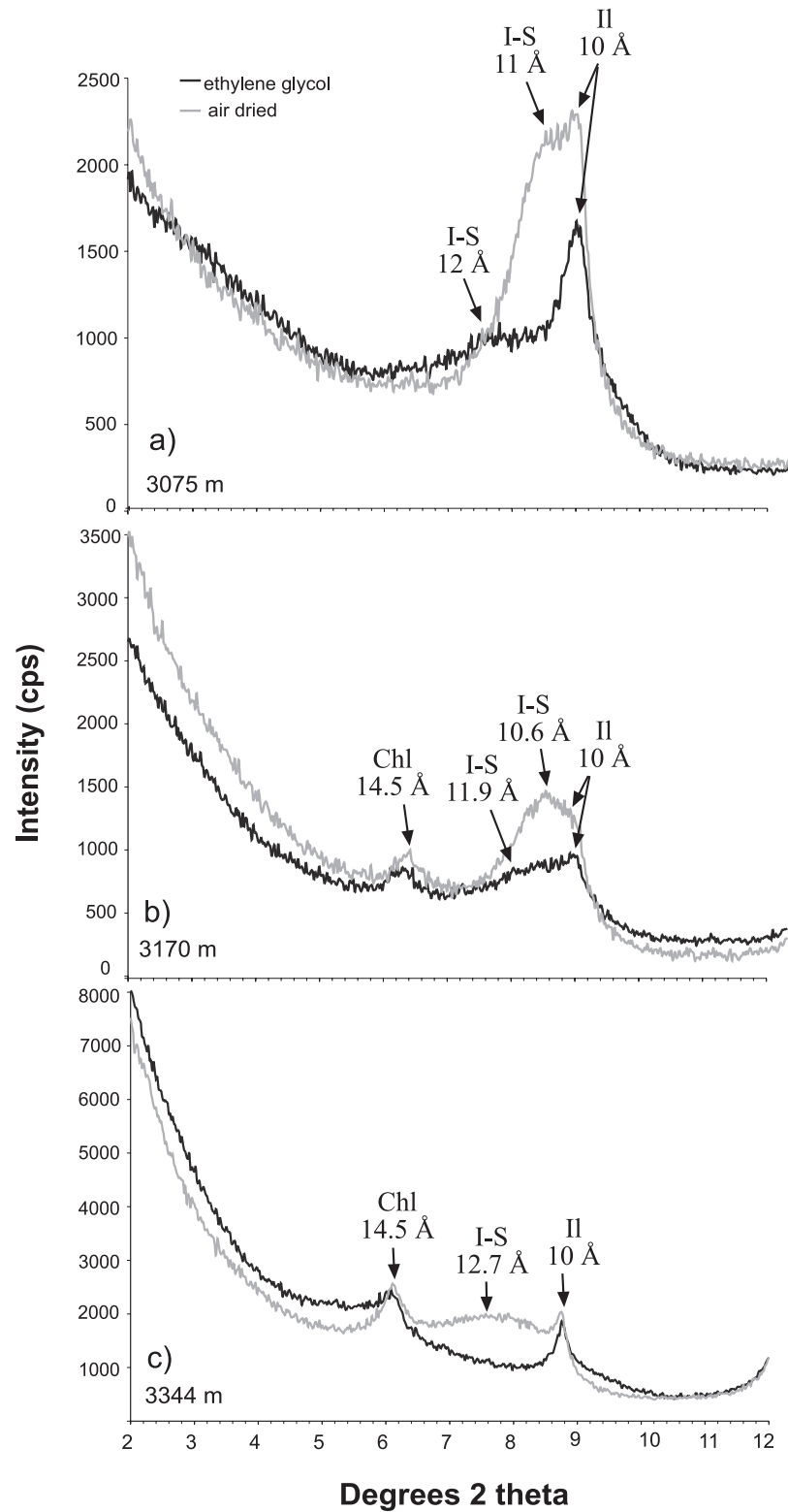
**Figure 2.** X-ray diffraction patterns from plucked fault rock cuttings at (a) 3075 m MD, (b) 3170 m MD, and (c) 3344 m MD. Air-dried and glycolated spectra are shown. Chl, chlorite; I-S, illite-smectite; Il, illite.
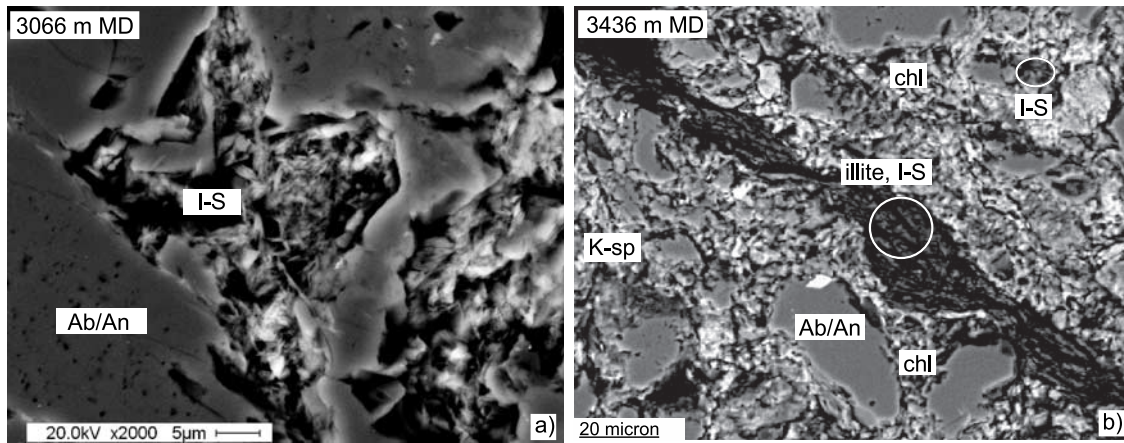
**Figure 3.** Backscattered scanning electron microscopy images of mudrocks from (a) 3066 m MD and (b) 3436 m MD. I-S mineralization in pores, veins, and sutured grain boundaries make up the fine-grained matrix of clastic lithologies. Ab/An, albite-anorthite; I/S, illite-smectite; Chl, chlorite; Qtz, quartz; K-spa, potassium feldspar.
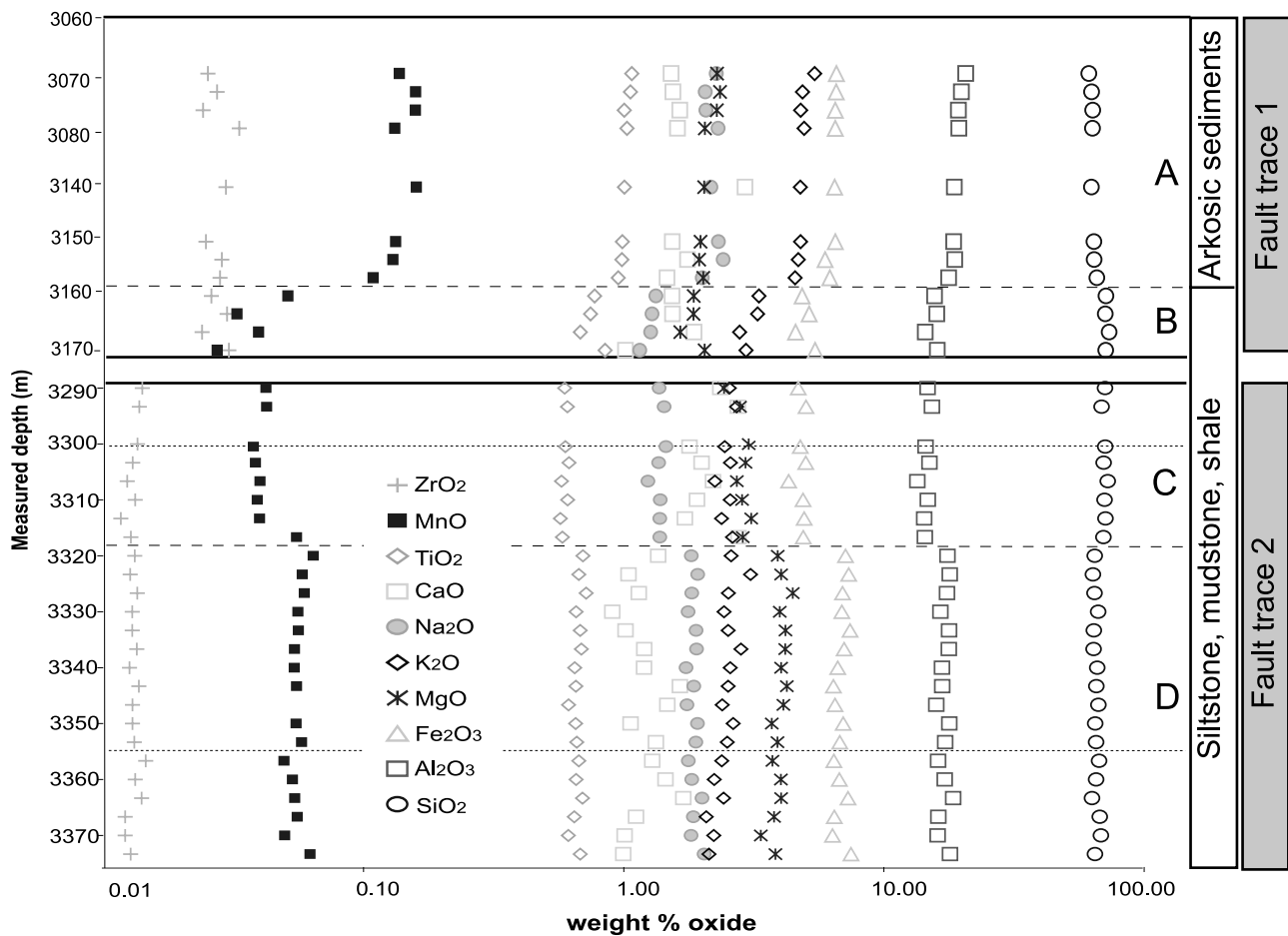


**Figure 4.** Elemental concentrations of picked faulted mudrock lithologies from SAFOD cuttings plotted against depth. The oxides are presented in order of increasing abundance. (a–d) Dashed lines represent main changes in elemental distribution. Note the area of gas peaks [*Wiersberg and Erzinger*, 2007] and casing deformation at 3301 m MD ([*Zoback and Hickman*, 2005]; gray dotted line). Bars on the right represent the lithology changes and the two fault zones (shallow fault trace 1 and deep main fault trace 2) examined in the study (see also Figure 1). Solid line represents break between shallow and deep fault.

basis of TEM observations some very small veins are also filled with smectitic minerals [*Schleicher et al.*, 2006b].

## 4.2. Geochemistry

### 4.2.1. Major Element Distribution

[15] A composite traverse through the fault zone is plotted using a logarithmic scale in Figure 4. It shows the elemental distribution of the picked fault-related grains across the shallow fault and the deep fault traces. The most constant concentrations in both fault zones are seen for $SiO_2$, $Al_2O_3$, and $ZrO_2$. In the shallow fault trace 1, the oxide element distributions are all relatively homogenous with one distinct change at 3160 m MD. Beneath this level, MnO, $TiO_2$, $Na_2O$, MgO, $K_2O$, and $Fe_2O_3$ are slightly more depleted, whereas some oxides (MnO, $TiO_2$, $Na_2O$, and $K_2O$) show a continuous decrease until 3170 m MD. Only CaO is more enriched after the change at 3160 m MD, and shows a continuous increase with depth.

[16] In comparison to the shallow fault trace 1, the deeper fault trace 2 shows notably lower concentrations of $ZrO_2$, MnO, $TiO_2$, $K_2O$, and $Na_2O$ oxides in the fault-related grains, a higher fluctuation of CaO and enrichment in MgO oxides. The consistent concentration of $SiO_2$, $Al_2O_3$, and $Fe_2O_3$ indicate a largely isovolumetric alteration through the entire depth [*Yonkee et al.*, 2003], but with two minor changes at ~3318 m MD and 3365 m MD. The depths at 3318 m correspond to the recently active main fault trace that has been determined from logging data, casing deformation [*Zoback and Hickman*, 2005] and gas analyses [*Wiersberg and Erzinger*, 2007, 2008]. Whereas ZrO and $K_2O$ show no distinct changes at 3318 m MD, $SiO_2$, and CaO show further depletion and fluctuation, and $TiO_2$, $Al_2O_3$, MnO, $Na_2O$, MgO, and $Fe_2O_3$ increase. At the 3365 m MD boundary, $TiO_2$, $Na_2O$, MgO, $Fe_2O_3$, $Al_2O_3$, and $SiO_2$ decrease again, whereas MnO does not change, and $K_2O$ shows depletion. These two boundaries within the deeper fault trace most probably reflect a change in fluid-rock interaction, based on distinct fluid flow and different degrees of mineral dissolution and precipitation.

[17] The major element distributions in fault-related grains and bulk rock are illustrated in Figure 5, with $Al_2O_3$, CaO, $Fe_2O_3$, $K_2O$, $MgO_2$, and $Na_2O$ plotted against $SiO_2$ (Table 2). In fault trace 1 (Figure 5a) and fault trace 2 (Figure 5b), the difference in major element deviation of the fault-related grains from the average compositions of the bulk wall rock reflect the strong alteration and dissolution-precipitation processes occurring in these rocks. In fault trace 1, the concentration of $Al_2O_3$, $Fe_2O_3$, MgO, and $K_2O$ is, in general, higher in the fault-related grains than in the bulk wall rock, whereas CaO and $Na_2O$ show lower amounts. $SiO_2$ is always enriched in the wall rock samples, a trend that can also be recognized in fault trace 2 (Figure 5b). Here, the concentration of $Al_2O_3$, $Fe_2O_3$ is also higher in the fault-related grains, whereas there is no significant difference in the $K_2O$ and MgO concentrations recognizable. Again, the CaO and $Na_2O$ concentrations are lower in the fault-related grains than in the bulk wall rocks, similar to fault trace 1.

### 4.2.2. Isocon Analysis

[18] The balance of element transport between fault rock fragments and associated bulk wall rock can be assessed by isocon graphs that are constructed by using Gresens' equation [*Gresens*, 1967; *Grant*, 1986]. The diagrams in Figure 6 show the relative loss and gain of elements by plotting the average composition of the fault-related grains against the average bulk rock samples throughout the fault zone [*Grant*, 1986, 2005]. In all diagrams, $TiO_2$ and ZrO define a line with an intermediate slope, suggesting that they behaved as immobile elements, which is a common assumption for rocks at these depths and in agreement with published data [*Baumgartner and Olsen*, 1995; *McCaig*, 1997; *Manatschal et al.*, 2000]. Applying the assumptions that (1) the fault rock and wall rock originate from the same protolith and have the same diagenetic state prior to faulting, (2) relative homogeneity of the protolith exists, and (3) density variations for the transition of fault rock to wall rock are insignificant, estimates on the degree of gain or loss of elements can be made [*Gresens*, 1967; *Ague and van Haren*, 1996; *Manatschal et al.*, 2000; *Grant*, 2005]. Normalizing to weight % oxides has a minimal effect on the mass balance calculations and satisfies the closure constraint. In our study the above assumptions are considered to be met, because of the low degree of variation observed for the main oxide components ($SiO_2$, $Al_2O_3$). Thus closure effects are minimal, and the high degree of similarity observed between the fine-grained wall rock and fault rock samples is supportive of consistent density and sample heterogeneity. However, as the assumptions cannot be otherwise confirmed, the quantification of element transport and the degree of fluid-rock interaction can represent only estimates. Table 1 summarizes the total calculated mass transport, mass transport per oxide and the average compositions for the fault rock and wall rock that were used in the calculation. The percent change for each element is also listed in Table 1.

[19] Considering $ZrO_2$ and $TiO_2$ to be immobile, the fault-related grains between 3066 and 3158 m MD show the highest degree of element depletion (Figure 6a). $TiO_2$ and $ZrO_2$ fall on the isocon together with $Rb_2O$, MnO, and MgO, showing similar immobility. Only $P_2O_5$ is slightly enriched in the fault rock. The isocon plot indicates clearly that $SiO_2$, $Al_2O_3$, $Na_2O$, CaO, $K_2O$, $Fe_2O_3$, and BaO are mobile phases in the system and these represent the main elements depleted during alteration and fault rock formation. The isocon slope of 2.4 for the shallowest part of the fault indicates a mass loss of ~58% between the wall rock and fault rock for this section.

[20] At 3160−3170 m MD, where a lithologic change appears with mudstone/shale/siltstone units, less mass transport occurs (Figure 6b). The isocon slope of 1.4 equates to a mass loss of 29%. Whereas $TiO_2$ and $ZrO_2$ again fall along the isocon line in accordance with immobile behavior, $Rb_2O$, MnO, $P_2O_5$, and MgO plot close to the isocon, indicating minor depletion in this area. $Al_2O_3$, $K_2O$, and $Fe_2O_3$ similarly lie beneath the isocon, but less than in the shallower section.

[21] The isocon for the first section of fault trace 2 (3292 m−3316 m MD, Figure 6c), lying above the main fault, has a slope of 1.6, indicating a minimum mass loss of ~38% between wall rock and fault rock. The depleted, mobile elements include $SiO_2$, $Al_2O_3$, $Na_2O$, CaO, $K_2O$, $Fe_2O_3$, MgO, MnO, and BaO, whereas $Rb_2O$ and $P_2O_5$ also lie on the isocon. The isocon for the deepest section (3320 m−3368 m MD, Figure 6d), beneath the main fault,
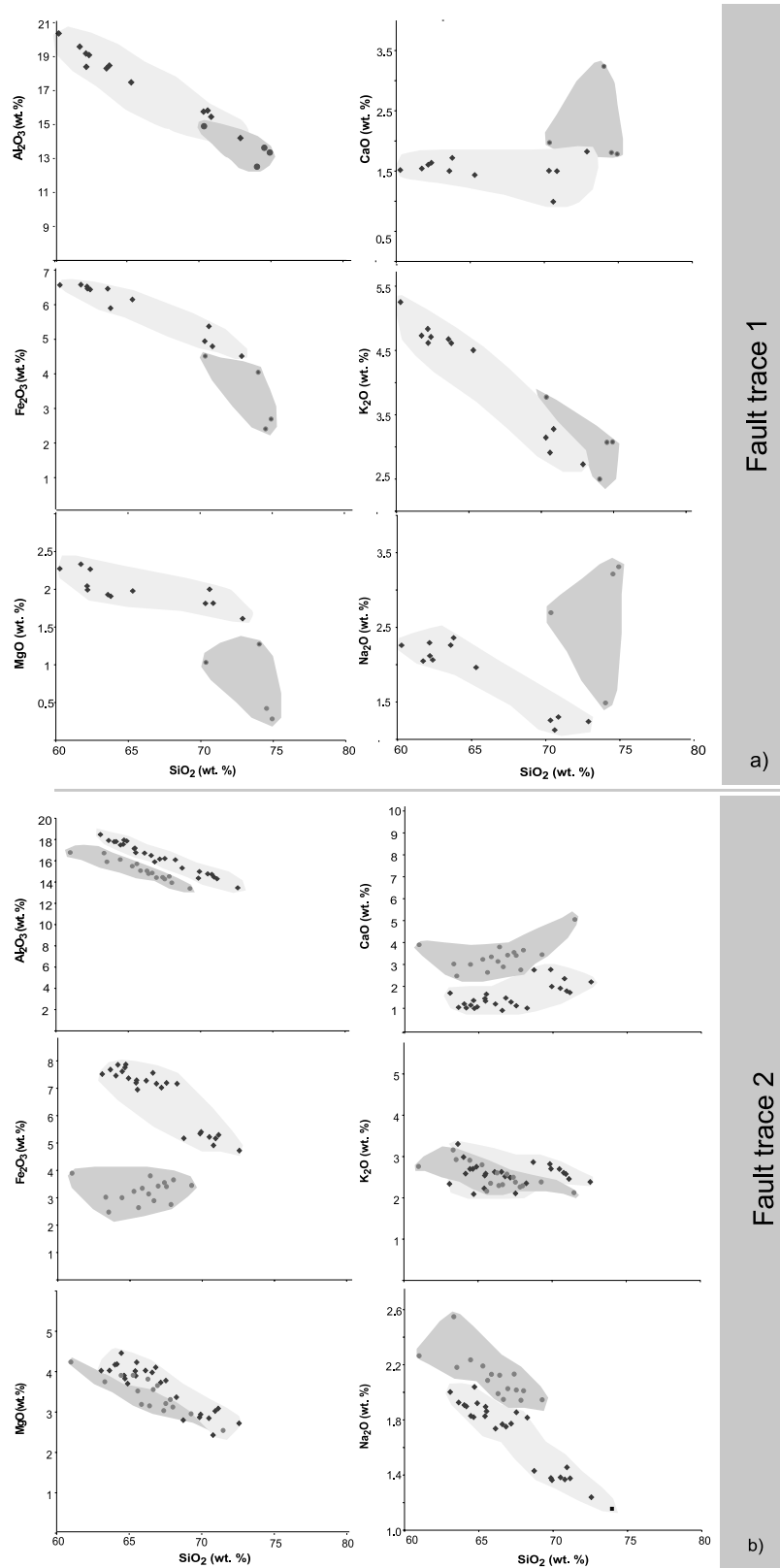
**Figure 5.** Major element comparisons from (a) 3069 m to 3170 m MD and (b) 3292–3368 m MD over $SiO_2$ wt % to evaluate relative mobility during alteration. Circles represent whole rock and diamonds represent picked fault rock.

**Table 2.** Average Weight % Oxide Composition of the Four Sections Investigated

| | 3069–3158 m | | 3161–3170 m | | 3292–3316 m | | 3319–3368 m | |
|---|---|---|---|---|---|---|---|---|
| | Average Picked Fault Rock (wt %) | Average Bulk Rock (wt %) | Average Picked Fault Rock (wt %) | Average Bulk Rock (wt %) | Average Picked Fault Rock (wt %) | Average Bulk Rock (wt %) | Average Picked Fault Rock (wt %) | Average Bulk Rock (wt %) |
| Al2O3 | 18.86 | 13.96 | 15.31 | 12.52 | 14.55 | 9.68 | 17.15 | 13.43 |
| BaO | 0.05 | 0.25 | 0.04 | 0.15 | 0.04 | 0.09 | 0.04 | 0.08 |
| CaO | 1.73 | 1.85 | 1.46 | 3.24 | 2.19 | 4.42 | 1.23 | 2.83 |
| Fe2O3 | 6.30 | 3.21 | 4.91 | 4.05 | 4.82 | 4.20 | 6.87 | 5.17 |
| K2O | 4.79 | 3.31 | 3.02 | 2.50 | 2.51 | 1.89 | 2.47 | 2.27 |
| MgO | 2.09 | 0.58 | 1.81 | 1.27 | 2.84 | 2.26 | 3.97 | 3.21 |
| MnO | 0.14 | 0.05 | 0.04 | 0.05 | 0.04 | 0.07 | 0.06) | 0.07 |
| Na2O | 2.17 | 3.07 | 1.23 | 1.49 | 1.37 | 1.46 | 1.86 | 1.80 |
| P2O5 | 0.13 | 0.02 | 0.23 | 0.17 | 0.46 | 0.24 | 0.18 | 0.17 |
| Rb2O | 0.02 | 0.01 | 0.01 | 0.01 | 0.01 | 0.01 | 0.01 | 0.01 |
| SiO2 | 62.68 | 73.33 | 71.17 | 74.03 | 70.55 | 75.27 | 65.44 | 70.49 |
| TiO2 | 1.00 | 0.33 | 0.74 | 0.51 | 0.59 | 0.33 | 0.66 | 0.46 |
| ZrO2 | 0.03 | 0.01 | 0.03 | 0.02 | 0.01 | 0.01 | 0.01 | 0.01 |
| Sum | 100.00 | 100.00 | 100.00 | 100.00 | 99.99 | 99.97 | 99.96 | 99.99 |

has a slope of 1.2, representing a mass loss of ~17% between wall rock and fault rock. Most of the elements plot close to the isocon, with CaO and BaO appearing to be the most mobile elements in the system.

## 5. Discussion

### 5.1. Mineralogical and Geochemical Effects

[22] Our investigation of drill cuttings from fault traces 1 and 2 of the SAFOD drill hole (3066–3169 m and 3292–3368 m MD), which represent areas of multiple alteration and deformation and includes recent active casing deformation at 3301 m MD [*Bradbury et al.*, 2007; *Zoback et al.*, 2005], indicates that extensive fluid-rock interaction occurred in the fault rocks. Using the temperature measurements from today's SAFOD drill hole of ~110–114°C [*Williams et al.*, 2005], the elemental mass balance and the molar (moles/kg) silica solubility was calculated on the basis of *Gresens*' [1967] equations (Figure 6 and Table 2).
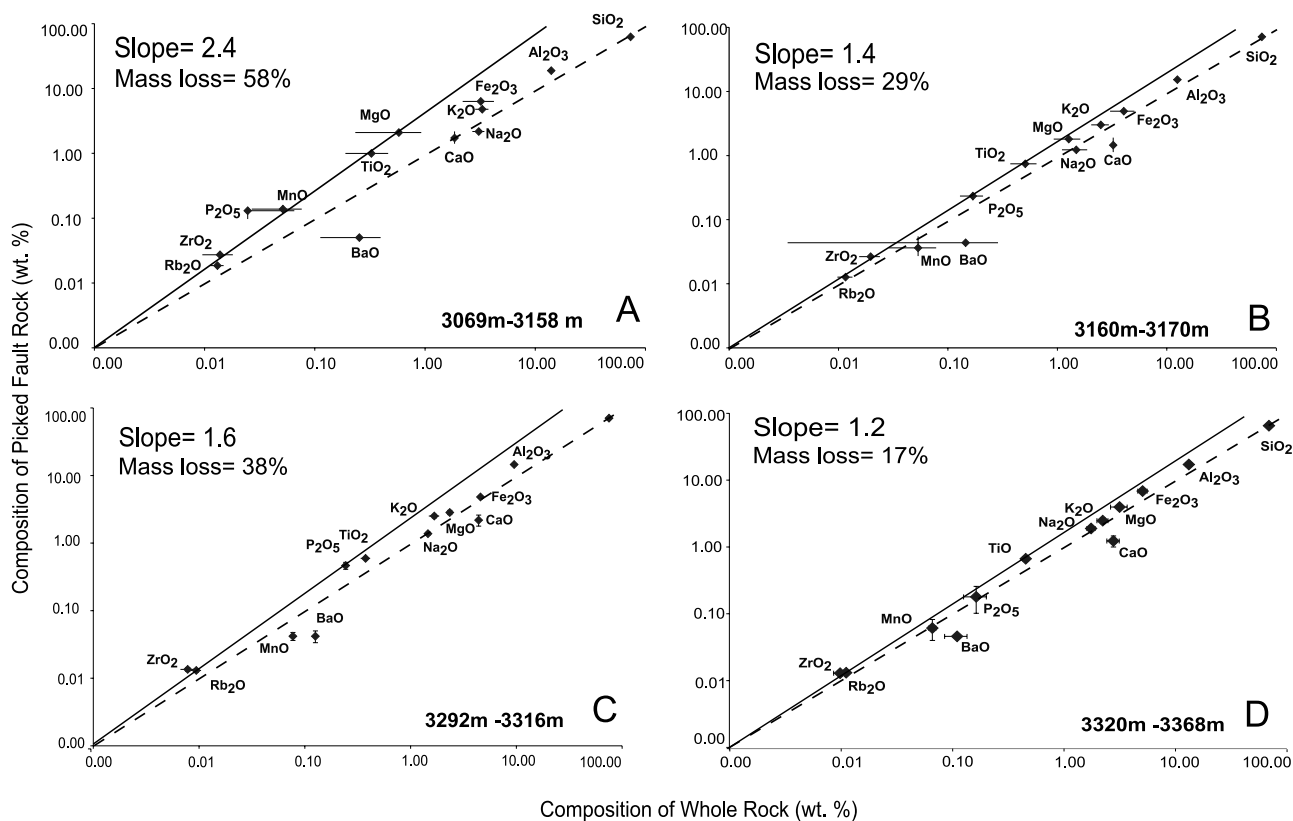


**Figure 6.** Isocon diagrams for the shallow fault trace 1 (Figures 4a and 4b) and the deep fault trace 2 (Figures 4c and 4d) of the San Andreas Fault. Error bars are shown on the basis of 1 standard deviation. The slopes of the isocons are calculated using $TiO_2$ and $ZrO_2$ as immobile elements. 1:1 slopes are shown as dashed lines.

Converting the $SiO_2$ wt % oxide to moles of $SiO_2$ and using the molar solubility of silica, the fluid-rock ratios are calculated on the basis of *Rimstidt*'s [1997] equation, ranging from 47 to 141 at the current temperatures. These high ratios show that both fault traces experienced extensive circulation of hydrous fluids that account for the progressive dissolution and leaching during faulting. The high quartz solubility may be a fault-related process and an explanation of the lack of quartz veins in the SAFOD rocks. We also note that, as the bulk rock samples include both detrital minerals and fault rock grains, these calculations provide only minimum estimates, so the actual effects may be even greater.

## 5.2. Implications for Fluid-Rock Interaction

[23] The clay mineral analyses, microstructural observations, and the elemental distribution of fault-related grains and bulk rock material presented in this study show that significant dissolution-precipitation reactions occurred in both fault sections (trace 1 and 2) with enhanced, fluid-assisted element transport. Dissolution of primary quartz, feldspar, and mica led to elemental transport of Si, Al, K, Ca, Mg, and Fe, and the precipitation of mixed-layered I-S and C-S, calcite, and laumontite predominantly along fracture and fault surfaces. The loss of the alkali's ($K_2O$, CaO, $Na_2O$, $Al_2O_3$, and $SiO_2$) is generally linked to feldspar and quartz dissolution that can be observed in the SEM images (Figure 3). The minor loss of MgO and greater loss of $Fe_2O_3$ support the precipitation of chlorite and C-S. A likely interpretation is that the alkali elements were transported along slip surfaces and crystallized elsewhere in the form of I-S, C-S, and smectite minerals. Ca is highly mobile throughout the entire fault zone and likely contributed to the precipitation of Ca-zeolites, Ca-sulfates, and calcite. These precipitates are common in cuttings and core material [*Solum et al.*, 2006; *Bradbury et al.*, 2007; *Draper et al.*, 2005], and their abundance fluctuates across the fault traces occurring as vein or adjacent pore fillings. Another distinct Ca source is the alteration of anorthite, whereas the loss of K generally reflects the dissolution of detrital K-feldspar, biotite, or authigenic illite-smectite minerals that were formed during prior diagenesis.

[24] On the basis of detailed mineralogical study and modeling of I-S minerals in the matrix of several fine-grained mudrock core samples at three different depths, *Schleicher et al.* [2009] concluded that the bulk volume clay minerals formed during slow burial diagenesis over the past 5 to 11 Ma and are not necessarily related directly to fault slip. Exceptions to this burial pattern are the mixed layered phases with higher smectite content than predicted by this burial model, which are concentrated along the mineralized slip surfaces that characterize the fault rock fragments analyzed in this study. As both burial- and fault-related clay are present to varying extent in both fault rock fragments and the less deformed host rock, it is evident that the elemental variations shown in Figure 6 result from a combination of these two processes.

[25] In this study, we distinguish three distinct changes in element composition through fault trace 1 and 2 (Figure 4). The change in the shallow fault may be explained by a lithologic transition from arkosic sandstone to fine-grained shaly rocks [*Bradbury et al.*, 2007]. However, because the picked fault-related grains with striations and polished surfaces are relatively homogenous in composition, showing only the appearance of chlorite in XRD, the continuous element depletion after 3160 m MD could also reflect enhanced fluid flow along the fault zone and higher degrees of fluid-rock interaction in this area. The clay mineral assemblage in fault trace 2 is relatively constant through depth with no lithologic variation, but two recognizable changes in the concentration of elements occur at 3317 m MD and at 3355 m MD. Here *Wiersberg and Erzinger* [2007] showed differences in the noble gas content of mud-gas samples, and *Zoback et al.* [2005] described distinct casing deformation at this level due to active fault creep. The concentrations of $TiO_2$, $Mn_2O_3$, MgO, $Fe_2O_3$, $Na_2O$, and $Al_2O_3$ and the strong fluctuation of CaO can be attributed to the enhanced precipitation of chlorite and/or C-S minerals. At 3368 m MD, another slight change in elemental distribution corresponds with small but notable gas peaks. These variations are likely related to the dissolution of minerals induced by disequilibrium between the fluid and the wall rock. Local dissolution occurs in association with brittle fracturing and mineralization on slip surfaces, whereby stress-induced mineral dissolution and reprecipitation at grain-contacts are mechanisms that can facilitate active fault creep. These relationships imply a genetic relationship between the degree of elemental transfer and local creep zones within the fault core.

[26] As it can be realistically assumed that the degree of diagenetic alteration prior to faulting was similar for the same lithologies at similar depths, the isocon plots can be used to estimate the degree of fluid-rock interaction incurred during the faulting. The highest degree of fluid-rock interaction recorded from the depth above ~3160 m (area A of Figure 4), with the highest mass loss of 58% and a high fluid/rock ratio of 141, may correspond to the more permeable fractured fault margin as identified by *Wiersberg and Erzinger* [2008]. However, as not all gas data are available between 3060 and 3160 m MD, the precise position of the upper fault core boundary remains uncertain.

[27] The lowest degree of element depletion recorded in the fault rock compared to the wall rock lithology occurs in the deepest part of fault trace 2, between 3320 and 3368 m MD with ~17% of mass loss and fluid/rock ratio of 47 (Figure 6d). This corresponds to the depth of active fault creep with recent casing deformation [*Zoback et al.*, 2005], element changes at 3317 m MD and 3355 m MD, and significant in situ gas peaks in the drilling mud [*Wiersberg and Erzinger*, 2008]. Here I-S and C-S are the main alteration products in the fault fragments. Whereas the precipitation of C-S may be triggered by the transportation of Mg and Fe from the wall rock into the fault rocks, K, and Ca are leading elements for precipitation of I-S minerals as thin films on fracture surfaces. The reduced amount of fluid migration is likely related to the higher amount of thin film coatings containing clays with greater amounts of interlayered smectite that precipitate on fracture surfaces [*Schleicher et al.*, 2006b] and not in the wall rock. Stress-enhanced dissolution at grain contacts is therefore proposed as the main mechanism for mineral transformation in these fault rocks, based on the localization of neomineralization on slip surfaces.

[28] The high degree of fluid-rock interaction within the segments of the fault zone is further supported by the detection of recent fluids of Na-Ca-Cl composition in the SAFOD borehole, which are considered to be typical formation waters for sedimentary rocks in California [*Thordsen et al.*, 2005]. The present-day borehole temperatures (~110°C and ~114°C respectively) are ideal for extensive leaching and clay mineral precipitation. However, on the basis of in situ mud-gas analysis in the Pilot and Main boreholes, *Wiersberg and Erzinger* [2007, 2008] suggested that the San Andreas Fault acts as a barrier for both horizontal and vertical fluid flow, with more permeable rocks at the fault zone margins surrounding a low-permeable fault core. The distinct gas composition of some sections detected in the fault at ~3150–3200 m and 3310–3340 m were interpreted as isolated gas lenses trapped from the surrounding source rocks.

[29] Our results partly support the model of *Wiersberg and Erzinger* [2007], with a higher degree of fluid/rock interaction occurring along the margins of the fault core than within the core itself. However, the geochemical constraints on the degree of elemental depletion along the principal fault traces clearly indicate that the San Andreas Fault zone has not behaved as an impermeable structure. The mass loss and fluid-rock ratios we calculated require significant volumes of paleofluid along the fault during its history of development. Such discrepancies are to be expected in seismically active fault zones, which represent dynamically evolving structures that experience rapid changes in stress, permeability, and fluid flow linked to the earthquake cycle [*Sibson*, 1994]. Given today's state of a fault that is not transporting much fluid, we suggest the core of the structure is currently in a stage of mineralization as opposed to transient fluid flow. The passage of such fluids still remains the primary cause of mineral hydration and clay growth within this active portion of the fault zone, and is an important agent in mass transfer and weakening during San Andreas faulting.

## References

Abbey, S. (1983), Studies in "standard samples" of silicate rocks and minerals 1969–1982, *Pap. Geol. Surv. Can., 83–15*, 114 pp.

Ague, J. J., and J. L. M. van Haren (1996), Assessing metasomatic mass and volume changes using the bootstrap, with application to deep crustal hydrothermal alteration of marble, *Econ. Geol., 91*, 1169–1182.

Baumgartner, L. P., and S. N. Olsen (1995), A least-squares approach to mass transport calculations using the isocon method, *Econ. Geol., 90*, 1261–1270.

Beach, A. (1976), The interrelations of fluid transport, deformation, geochemistry and heat flow in early Proterozoic shear zones in the Lewisian Complex, *Philos. Trans. R. Soc. London, Ser. A, 280*, 569–604.

Bradbury, K. K., D. C. Barton, J. G. Solum, S. D. Draper, and J. P. Evans (2007), Mineralogic and textural analyses of drill cuttings from the San Andreas Fault Observatory at Depth (SAFOD) boreholes: Initial interpetations of fault zone composition and constraints on geologic models, *Geosphere, 3*(5), 299–318, doi:10.1130/GES00076.1.

Carter, N. L., A. K. Kronenburg, J. V. Ross, and D. V. Wiltscho (1990), Control of fluids on deformation in rocks, in *Deformation Mechanisms, Rheology and Tectonics*, edited by R. J. Knipe and E. H. Rutter, *Geol. Soc. Spec. Publ., 54*, 1–13.

Chester, F. M., and J. M. Logan (1986), Implications for mechanical properties of brittle faults from observations of the Punchbowl Fault zone, California, *Pure Appl. Geophys., 124*, 79–106, doi:10.1007/BF00875720.

Crawford, B. R., R. D. Myers, A. Woronow, D. R. Faulkner, and E. H. Rutter (2002), Porosity-permeability relationships in clay-bearing fault gouge, SPE paper 78214 presented at Rock Mechanics Conference, Irvin, Tex., 1–13.

Dewhurst, D. N., Y. Yang, and A. C. Aplin (1999), Permeability and fluid flow in natural mudstones, in *Muds and Mudstones: Physical and Fluid Flow Properties*, edited by A. C. Aplin et al., pp. 23–45, Geol. Soc. London, U. K.

Draper, S. D., N. L. Boness, and J. P. Evans (2005), Source and significance of the sedimentary rocks in the SAFOD borehole: Preliminary analysis, *Eos Trans. AGU, 86*(52), Fall Meet. Suppl., Abstract T24B–02.

Evans, J. P., and F. M. Chester (1995), Fluid-rock interaction in faults of the San Andreas system: Inferences from San Gabriel Fault rock geochemistry and microstructures, *J. Geophys. Res., 100*, 13,007–13,020, doi:10.1029/94JB02625.

Flanagan, F. J. (1976), Descriptions and analyses of eight new USGS rock standards, *U.S. Geol. Surv. Prof. Pap., 840*, 192.

Forster, C. B., and J. P. Evans (1991), Fluid flow in thrust faults and crystalline thrust sheets: Results of combined field and modeling studies, *Geophys. Res. Lett., 18*, 979–982, doi:10.1029/91GL00950.

Gladney, E. S., and I. Roelandts (1988), Compilation of elemental concentration data for USGS BHVO-1, MAG-1, QLO-1, RGM-1, SCo-1, SDC-1, SGR-1, and STM-1, *Geostand. Newsl., 12*, 253–362, doi:10.1111/j.1751-908X.1988.tb00053.x.

Govindaraju, K. (1994), Compilation of working values and descriptions for 383 geostandards, *Geostand. Newsl., 18*, 1–158.

Grant, J. A. (1986), The isocon diagram: A simple solution to Gresens' equation for metasomatic alteration, *Econ. Geol., 81*, 1976–1982.

Grant, J. A. (2005), Isocon analysis: A brief review of the method and applications, *Phys. Chem. Earth, 30*, 997–1004.

Gresens, R. L. (1967), Composition-volume relationships of metasomatism, *Chem. Geol., 2*, 47–65, doi:10.1016/0009-2541(67)90004-6.

Hayman, N. W. (2006), Shallow crustal fault rocks from the Black Mountain detachments, Death Valley, CA, *J. Struct. Geol., 28*, 1767–1784, doi:10.1016/j.jsg.2006.06.017.

Hickman, S. H., and M. D. Zoback (2004), Stress orientation and magnitudes in the SAFOD Pilot hole, *Geophys. Res. Lett., 31*, L15S12, doi:10.1029/2004GL020043.

Hickman, S. H., M. D. Zoback, and W. L. Ellsworth (2004), Introduction to special section: Preparing for the San Andreas Fault Observatory at Depth, *Geophys. Res. Lett., 31*, L12S01, doi:10.1029/2004GL020688.

Hickman, S. H., M. D. Zoback, and W. L. Ellsworth (2005), Structure and composition of the San Andreas Fault zone at Parkfield: Initial results from SAFOD Phase I and II, *Eos Trans. AGU, 86*(52), Fall Meet. Suppl., Abstract T23E–05.

Hickman, S., et al. (2008), Structure and composition of the San Andreas Fault in central California: Recent results from SAFOD sample analyses, *Eos Trans. AGU, 89*(53), Fall Meet. Suppl., Abstract T53F–01.

Hulsebosch, T. P., and B. R. Frost (1989), Mineral changes, element mobility, and fluids associated with deep shearing in the Mount Helen structural belt, in *Fluid Movements, Element Transport and the Composition of the Deep Crust, NATO Sci. Ser., Ser. C Mathematical and Physical Sciences*, vol. 281, edited by D. Bridgewater, pp. 139–150, Kluwer Acad., Dordrecht, Netherlands.

Manatschal, G., D. Marquer, and G. L. Frueh-Gree (2000), Channelized fluid flow and mass transfer along a rift-related detachment fault (eastern Alps, southeast Switzerland), *Geol. Soc. Am. Bull., 112*(1), 21–33, doi:10.1130/0016-7606(2000)112<0021:CFFAMT>2.3.CO;2.

Marquer, D., and M. Burkhard (1992), Fluid circulation, progressive deformation and mass-transfer processes in the upper crust: The example of basement-cover relationships in the External Crystalline Massifs, Switzerland, *J. Struct. Geol., 14*, 1047–1057, doi:10.1016/0191-8141(92)90035-U.

McCaig, A. M. (1984), Fluid-rock interaction in some shear zones from the Pyrenees, *J. Metamorph. Geol., 2*, 129–141, doi:10.1111/j.1525-1314.1984.tb00292.x.

McCaig, A. M. (1997), The geochemistry of volatile fluid flow in shear zones, in *Deformation-Enhanced Fluid Transport in the Earth's Crust and Mantle, Mineral. Soc. Ser.*, vol. 8, edited by M. B. Holness, pp. 227–266, Chapman and Hall, London.

Moore, D. M., and R. C. Reynolds Jr. (1997), *X-Ray Diffraction and the Identification of Clay Minerals*, 2nd ed., Oxford Univ. Press, Oxford, U. K.

Rimstidt, J. D. (1997), Quartz solubility at low temperatures, *Geochim. Cosmochim. Acta*, *61*, 2553–2558, doi:10.1016/S0016-7037(97)00103-8.

Schleicher, A. M., L. N. Warr, and B. A. van der Pluijm (2006a), Fluid focusing and back-reactions in the uplifted shoulder of the Rhine rift system: A clay mineral study along the Schauenburg Fault zone (Heidelberg, Germany), *Int. J. Earth Sci.*, *95*(1), 19–33, doi:10.1007/s00531-005-0490-3.

Schleicher, A. M., B. A. van der Pluijm, and L. N. Warr (2006b), Origin and significance of clay-coated fractures in mudrock fragments of the SAFOD borehole (Parkfield, California), *Geophys. Res. Lett.*, *33*, L16313, doi:10.1029/2006GL026505.

Schleicher, A. M., L. N. Warr, and B. A. van der Pluijm (2009), On the origin of mixed-layered clay minerals from the San Andreas Fault at 2.5–3 km vertical depth (SAFOD drillhole at Parkfield, California), *Contrib. Mineral. Petrol.*, *157*, 173–187, doi:10.1007/s00410-008-0328-7.

Schulz, S. E., and J. P. Evans (2000), Mesoscopic structure of the Punchbowl Fault, southern California and the geologic and geophysical structure of active strike-slip faults, *J. Struct. Geol.*, *22*, 913–930, doi:10.1016/S0191-8141(00)00019-5.

Sibson, R. H. (1994), Crustal stress, faulting and fluid flow, in *Geofluids: Origin, Migration and Evolution of Fluids in Sedimentary Basins*, edited by J. Parnell, *Geol. Soc. Spec. Publ.*, vol. 78, pp. 69–84.

Solum, J. G., and B. A. van der Pluijm (2004), Phyllosilicate mineral assemblages of the SAFOD Pilot hole and comparisons with an exhumed segment of the San Andreas Fault system, *Geophys. Res. Lett.*, *31*, L15S19, doi:10.1029/2004GL019909.

Solum, J. G., B. A. van der Pluijm, D. R. Peacor, and L. N. Warr (2003), Influence of phyllosilicate mineral assemblages, fabrics, and fluids on the behavior of the Punchbowl Fault, southern California, *J. Geophys. Res.*, *108*(B5), 2233, doi:10.1029/2002JB001858.

Solum, J. G., S. H. Hickman, D. A. Lockner, D. E. Moore, B. A. van der Pluijm, A. M. Schleicher, and J. P. Evans (2006), Mineralogical characterization of protolith and fault rocks from the SAFOD Main hole, *Geophys. Res. Lett.*, *33*, L21314, doi:10.1029/2006GL027285.

Thordsen, J. J., W. C. Evans, Y. K. Kharaka, B. M. Kennedy, and M. van Soestim (2005), Chemical and isotopic composition of water and gases from the SAFOD wells: Implications to the dynamics of the San Andreas Fault at Parkfield, CA, *Eos Trans. AGU*, *86*(52), Fall Meet. Suppl., Abstract T23E–08.

Tobin, H., P. Vannucchi, and M. Meschede (2001), Structure, inferred mechanical properties, and implications for fluid transport in the decollement zone, Costa Rica, convergent margin, *Geology*, *29*(10), 907–910, doi:10.1130/0091-7613(2001)029<0907:SIMPAI>2.0.CO;2.

Vrolijk, P., and B. A. van der Pluijm (1999), Clay gouge, *J. Struct. Geol.*, *21*, 1039–1048, doi:10.1016/S0191-8141(99)00103-0.

Wiersberg, T., and J. Erzinger (2007), A helium isotope cross-section study through the San Andreas Fault at seismogenic depths, *Geochem. Geophys. Geosyst.*, *8*(1), Q01002, doi:10.1029/2006GC001388.

Wiersberg, T., and J. Erzinger (2008), Origin and spatial distribution of gas at seismogenic depths of the San Andreas Fault from drill-mud gas analysis, *Appl. Geochem.*, *23*, 1675–1690, doi:10.1016/j.apgeochem.2008.01.012.

Williams, C. F., M. A. d'Alessio, F. V. Grubb, and S. P. Galanis Jr. (2005), Heat flow studies in the SAFOD Main hole, *Eos Trans. AGU*, *86*(52), Fall Meet. Suppl., Abstract T23E–07.

Wu, F. T., L. Blatter, and H. Roberson (1975), Clay gouges in the San Andreas Fault system and their possible implications, *Pure Appl. Geophys.*, *113*, 87–95, doi:10.1007/BF01592901.

Yonkee, W. A., W. T. Parry, and R. L. Bruhn (2003), Relations between progressive deformation and fluid-rock interaction during shear-zone growth in a basement-cored thrust sheet, Sevier orogenic belt, Utah, *Am. J. Sci.*, *303*, 1–59, doi:10.2475/ajs.303.1.1.

Zoback, M. D., and S. H. Hickman (2005), Preliminary observations of stress and fluid pressure in and near the San Andreas Fault at depth in SAFOD boreholes, *Eos Trans. AGU*, *86*(52), Fall Meet. Suppl., Abstract T21A–0438.

Zoback, M., S. Hickman, and W. Ellsworth (2005), Drilling, sampling and measurements in the San Andreas Fault zone at seismogenic depth, *Eos Trans. AGU*, *86*(52), Fall Meet. Suppl., Abstract T23E–01.

————————————

A. M. Schleicher, S. N. Tourscher, and B. A. van der Pluijm, Department of Geological Sciences, University of Michigan, 1100 N. University Avenue, Ann Arbor, MI 48109-1005, USA. (aschleic@umich.edu)

L. N. Warr, Institut für Geographie und Geologie, Ernst Moritz Arndt Universität Greifswald, Friedrich-Ludwig-Jahn-Strasse17a, D-17487 Greifswald, Germany.